ՀՀ ԳԱԱ Վ. ՀԱՄԲԱՐՁՈՒՄՅԱՆԻ ԱՆՎԱՆ ԲՅՈՒՐԱԿԱՆԻ ԱՍՏՂԱԴԻՏԱՐԱՆ

Խաչատրյան Միեր Հրաչյաի

Մեքենայական ուսուցման ալգորիթմների կիրառում բլազարների դասակարգման և դրանց ճառագայթման մոդելավորման համար

ՍԵՂՄԱԳԻՐ

Ա.03.02 - «Աստղաֆիզիկա, ռադիոաստղագիտություն»
մասնագիտությամբ ֆիզիկամաթեմատիկական գիտությունների թեկնածուի
գիտական աստիճանի հայցման ատենախոսության

ԵՐԵՎԱՆ - 2026

NAS RA Byurakan Astrophysical Observatory after V. Ambartsumian

Khachatryan Mher Hrachya

Application of Machine Learning Algorithms to Classify Blazars and Model Their Radiation

Thesis for the degree of candidate in physical and mathematical sciences in the specialization A.03.02 - “Astrophysics, radioastronomy”

SYNOPSIS

YEREVAN-2026

Ատենախոսության թեման հաստատվել է ՀՀ ԳԱԱ Վ. Համբարձումյանի անվան Բյուրականի աստղադիտարանի գիտական խորհրդում:

Գիտական ղեկավար՝

ֆ.մ.գ.դ. Նարեկ Սահակյան

Պաշտոնական ընդդիմախոսներ՝

ֆ.մ.գ.դ. Գագիկ Տեր-Ղազարյան
ֆ.մ.գ.թ. Գրիգոր Ալավերդյան

Առաջատար կազմակերպություն՝

Երևանի Պետական Համալսարան

Պաշտպանությունը կայանալու է 2026 թ.-ի հունիսի 22-ին ժամը 12:00-ին, ՀՀ ԳԱԱ Վ. Համբարձումյանի անվան Բյուրականի աստղադիտարանում, «Աստղաֆիզիկա, ռադիոաստղագիտություն» 048 մասնագիտական խորհրդում:

Ատենախոսությանը կարելի է ծանոթանալ ՀՀ ԳԱԱ Վ. Համբարձումյանի անվան Բյուրականի աստղադիտարանի գրադարանում:

Սեղմագիրը առաքված է 2026 թ.-ի մայիսի 15-ին:

Մասնագիտական խորհրդի գիտական քարտուղար՝ ֆ.մ.գ.թ. Հայկ Աբրահամյան

The thesis is approved by the scientific council of the NAS RA Byurakan Astrophysical Observatory after V. Ambartsumian.

Scientific advisor:

Doctor of Phys. Math. Sciences Narek Sahakyan

Official opponents:

Doctor of Phys. Math. Sciences Gagik Ter-Ghazaryan
Candidate of Phys. Math. Sciences Grigor Alaverdyan

Leading Organization:

Yerevan State University

The defense of the thesis will take place on June 22, 2026, at 12:00, on the session of the Special Council “Astronomy, radioastronomy” 048 of the NAS RA Byurakan Astrophysical Observatory after V. Ambartsumian.

The thesis is available in the library of the NAS RA Byurakan Astrophysical Observatory after V. A. Ambartsumian.

The synopsis is distributed on May 15, 2026.

Scientific secretary of the Special Council: Candidate of Phys. Math. Sciences Hayk Abrahamyan

General Description of the Thesis

Relevance of the topic

Blazars are Active Galactic Nuclei (AGN) which have relativistic jets that are viewed at small angles to the line of sight. Because of Doppler boosting, they appear as one of the most luminous and variable extragalactic sources, with non-thermal emission extending from radio frequencies to high-energy (HE) and sometimes very-high-energy (VHE) γ-rays. Their broadband spectral energy distributions (SEDs) usually show two broad components: a low-energy synchrotron component and a high-energy component that may be produced by inverse-Compton or hadronic processes.

Studying blazars is important for several reasons. First, they make it possible to test physics near supermassive black holes (SMBHs) and inside relativistic jets, where particle acceleration, radiative cooling, magnetic fields, and relativistic plasma dynamics are under extreme conditions. Second, the blazar emission is over a wide range of energy band, making them interesting objects for multiwavelength observations. Third, the association of some blazars with HE neutrino events makes them central sources in multimessenger astrophysics.

At the same time, detailed physical modeling of blazar SEDs is computationally expensive. Self-consistent radiative models require repeated calculations during parameter inference, which becomes difficult for large samples and for time-resolved studies containing many epochs. Another issue is that many blazar candidates lack statistically robust classifications into the two main subtypes based on optical spectra: flat-spectrum radio quasars (FSRQs) and BL Lacertae objects (BL Lacs). This limits blazar population studies and makes source selection for follow-up observational campaigns more difficult.

In recent years, machine learning methods have become powerful tools in astronomy and astrophysics, especially for problems involving large datasets and computationally expensive calculations. These methods are effective at finding hidden patterns in complex data, performing classification and regression tasks, estimating physical parameters, and approximating non-linear relationships between observables and underlying physical quantities. They can also be used as surrogate models to replace

slow numerical simulations with fast approximations, significantly reducing computation time and making large-scale and time-resolved studies feasible.

The aim of the thesis

The main goal of the thesis is to apply machine learning methods to improve the classification of blazars and to make the physical modeling of their broadband radiation more practical. The work keeps the analysis physically grounded by using observational features from *Fermi*-LAT catalogs and by training surrogate models on spectra generated from radiative calculations.

The main tasks are:

1. To classify blazar candidates of uncertain type (BCUs) in the *Fermi*-LAT 4FGL-DR3 catalog using observed γ-ray spectral and temporal properties.

2. To compare artificial neural networks with gradient-boosted decision tree methods, especially XGBoost and LightGBM, and identify a robust model for BCU subclass prediction.

3. To develop and validate a convolutional neural network (CNN) surrogate for one-zone synchrotron self-Compton (SSC) modeling of blazar SEDs.

4. To apply the trained SSC modeling framework to a large time-resolved study of PKS 2155-304.

5. To investigate the origin of the multiwavelength emission from the FSRQ PKS 1441+25 during different activity states, including the VHE-detected period.

Scientific novelty

The thesis presents several new results. A statistically grounded classification of BCUs in 4FGL-DR3 is obtained using 18 direct γ-ray observables and modern machine learning algorithms. It is shown that gradient-boosted tree methods are performing better for this catalog-scale problem because they handle small, heterogeneous, and partially incomplete tabular data efficiently. The classified candidate sources have properties statistically align with the properties of the identified objects, showing that

the classification algorithms can find and map the hidden physical properties with enough accuracy.

A second novel result is the construction of a fast CNN-based surrogate for a self-consistent one-zone SSC model. The network is trained on a large set of spectra generated with the kinetic code *SOPRANO*, including cooling and pair-production effects. This allows the model output to be evaluated approximately 1000 times faster than direct numerical calculations, while preserving the connection to the underlying physical model.

The trained network is then used to model 253 quasi-simultaneous SEDs of PKS 2155-304, providing a homogeneous multi-epoch view of how the magnetic field, electron luminosity, maximum electron energy, Doppler factor, and particle-acceleration conditions change in the jet across different activity states.

Finally, from the modeling of PKS 1441+25 it shows that its 2015 activity can be understood as an evolution of the emitting region along the jet: a compact, magnetically stronger region inside or near the broad-line region (BLR) in January, followed by larger particle-dominated regions beyond the BLR during April-June.

Practical importance

The statistical classification of BCUs improves the completeness and scientific usability of the *Fermi*-LAT blazar catalog by reducing the number of sources without subclass identification. This allows more reliable studies of the population properties, evolution, and luminosity distributions of BL Lacs and FSRQs using larger and more representative samples. In addition, the predicted subclasses help prioritize spectroscopic follow-up observations and improve source selection for multiwavelength campaigns and multimessenger studies, where the likely blazar subclass is often an important factor for scientific interpretation.

The CNN surrogate modeling framework significantly reduces the computational cost of fitting physically motivated SED models. Instead of requiring many seconds for a single direct numerical evaluation, the trained network can produce spectra in milliseconds, reducing full source modeling from days to minutes. This makes Bayesian inference and multi-epoch SED modeling feasible for sources with long-term monitoring and large numbers of observational epochs. Such an approach allows time-resolved studies that

would be impractical with direct numerical solvers alone.

Basic results to be defended

1. BCUs in the *Fermi*-LAT 4FGL-DR3 catalogue were classified using machine learning methods trained on 2219 confirmed BL Lac objects and FSRQs, described by 18 spectral and temporal parameters. Among the tested ANN, XGBOOST, and LIGHTGBM models, LIGHTGBM gave the best performance. The final classification assigned 825 BCUs as BL Lac candidates and 405 as FSRQ candidates, while 190 sources remained without a reliable class. This reduced the fraction of unclassified BCUs in 4FGL-DR3 to 5.1%. The classified sample was further used to study the connection between FSRQs and BL Lac subclasses through the γ-ray photon index, synchrotron peak frequency, and high-energy peak frequency.

2. CNN-based framework was developed for fast and self-consistent modeling of blazar SEDs. The CNN was trained on leptonic radiative models including synchrotron emission, inverse Compton scattering, electron cooling, and pair creation–annihilation processes. It is shown that the trained network reproduced the radiative output of the physical model with high accuracy while significantly reducing the computational time required for SED calculations. The method was combined with MultiNest to fit the broadband SEDs of Mrk 421 and 1ES 1959+650 and to derive posterior distributions of the model parameters. The developed framework enables efficient fitting of multiwavelength blazar data.

3. The temporal and spectral evolution of the blazar PKS 2155−304 was investigated using γ-ray, X-ray, optical/UV, and infrared observations. Multiwavelength light curves and 253 time-resolved SEDs were constructed to study the origin and variability of the emission. The source exhibited strong variability, particularly in the soft and medium X-ray bands, with significant variability also observed in the γ-ray band. The SEDs were modeled within a one-zone synchrotron self-Compton framework using a neural-network surrogate for rapid parameter estimation. Statistical analysis showed significant state-dependent variations of the physical parameters, including the magnetic field, electron luminosity, maximum electron Lorentz factor, Doppler factor,

and electron spectral index. The jet was found to be particle dominated with a magnetic-to-electron power ratio $\eta_B \simeq 0.09$–0.17, while X-ray flares showed increased magnetization. The results indicate that changes in particle acceleration efficiency and jet magnetization are responsible for the different flaring states observed in PKS 2155−304.

4. A multiwavelength analysis of the FSRQ PKS 1441+25 ($z = 0.939$) was performed. Adaptively binned γ-ray light curves revealed a prolonged high-activity period around MJD 57000, including a bright γ-ray flare in January 2015 and a hard spectrum in April coincident with VHE detections by MAGIC and VERITAS. SEDs corresponding to the January flare, the April VHE state, and the May–June quiescent states were modeled within a one-zone external inverse-Compton framework using CNN surrogate models for efficient parameter-space exploration. The April–June states were reproduced with weak magnetic fields and a large emitting region ($R \sim 10^{17}$ cm) located beyond the broad-line region, where dusty torus photons dominate and internal $\gamma\gamma$ absorption is negligible, allowing VHE photons to escape. In contrast, the January flare required a compact and more strongly magnetized region ($R \sim 10^{15}$ cm) located closer to the black hole, where disk and broad-line-region radiation fields dominate and suppress VHE emission through efficient $\gamma\gamma$ absorption. It is shown that the observed activity is mainly driven by the evolution and relocation of the dissipation region along the jet.

Approbation of the work

The results of the thesis were presented in Astroinformatics 2026 (February 23 – 27, 2026) as well as frequently presented and discussed at the seminars of ICRANet Armenia center.

Publications

Four articles related to the topic of the thesis have been published.

Structure of the thesis

The thesis consists of an introduction, five main sections, a conclusion, and a bibliography. The thesis contains 129 pages, 31 figures and 7 tables.

Content of the Thesis

Introduction

This section introduces blazars, presents the scientific motivation for studying blazars and explains why they are interesting targets for both multiwavelength astrophysical studies and machine learning-based analysis.

Chapter 1

Chapter 1 presents the theoretical and methodological background of the thesis. The main radiation mechanisms responsible for blazar emission, including synchrotron radiation, synchrotron self-Compton (SSC), external inverse Compton (EIC), and hadronic processes are presented. The characteristic two-component SEDs of blazars and the physical differences between BL Lac objects and FSRQs are also described. The chapter further summarizes the multiwavelength datasets and observatories used in the thesis, particularly Fermi-LAT, Swift, and the Markarian Multiwavelength Data Center (MMDC). In addition, it introduces the machine learning methods applied throughout the thesis. Gradient-boosted decision tree algorithms and artificial neural networks are discussed for the classification of blazars, while convolutional neural networks are presented as surrogate models for fast broadband SED modeling. The chapter explains how machine learning can both identify hidden patterns in observational data and significantly accelerate computationally expensive radiative calculations.

Chapter 2

In the second chapter, the classification of the large fraction of BCUs in the *Fermi*-LAT 4FGL-DR3 catalog is investigated. Since optical spectroscopy is not available for all candidate sources, 39.9% of the blazars in 4FGL-DR3 catalog remain BCUs. The thesis uses 18 direct γ-ray observables to predict whether a BCU is more likely to belong to the BL Lac or FSRQ subclass. Three different models are used: an artificial neural network (ANN), XGBoost, and LightGBM, with both default and optimized boosted-tree configurations.

The comparison of model performance is summarized in Table 1. For this catalog-scale classification problem, the gradient-boosted tree methods perform better than the neural-network baseline. In particular, the optimized

Table 1: The BCU classification performance of the models.

Model	Recall of Minority	Recall Weighted	Precision Weighted	ROC-AUC Macro
ANN	0.81	0.88	0.88	0.86
XGBoost_def	0.77	0.87	0.87	0.85
XGBoost_opt	0.80	0.87	0.87	0.86
LightGBM_def	0.81	0.87	0.87	0.86
LightGBM_opt	0.82	0.88	0.88	0.87

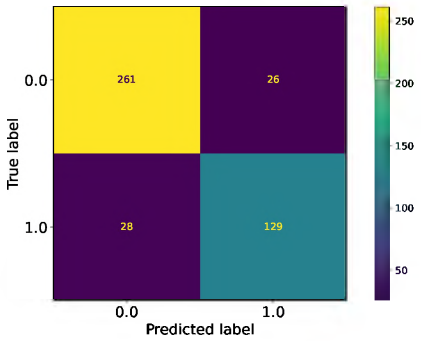

Figure 1: The confusion matrix of *LightGBM_opt* classifier on the test sample.

LightGBM model, *LightGBM_opt*, gives the best overall balance of metrics, reaching a minority-class recall of 0.82, weighted recall of 0.88, weighted precision of 0.88, and macro ROC–AUC of 0.87. Since the minority class is the FSRQ population, this result is important because it shows that the classifier is not simply driven by the more numerous BL Lac sources.

The behavior of the adopted classifier on the test sample is illustrated in Figures 1 and 2. The confusion matrix in Figure 1 shows that *LightGBM_opt* correctly classifies 261 BL Lacs and 129 FSRQs, while only 26 BL Lacs and 28 FSRQs are assigned to the wrong subclass. This nearly symmetric pattern of errors confirms that the model separates the two populations well and remains reliable even for the less represented FSRQ class. The ROC and precision–recall curves in Figure 2 provide a complementary view of the same result: the classifier maintains strong discrimination power over a broad range of thresholds, with a test-sample ROC–AUC of about 0.93 and a favorable balance between completeness and purity.

After selecting *LightGBM_opt* as the preferred classifier, asymmetric

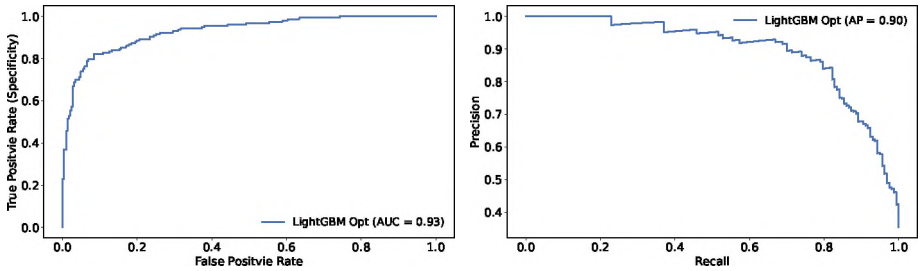

Figure 2: *Left panel:* ROC curve for *LightGBM_opt* classifier. *Right panel:* Precision Recall curve.

decision thresholds were adopted to improve the reliability of the assigned subclasses. A source is classified as a BL Lac candidate when $L_{\mathrm{BL\,Lac}} > 0.44$, and as an FSRQ candidate when $L_{\mathrm{FSRQ}} > 0.82$. This choice avoids forcing ambiguous objects into a class.

The thresholded classifier is then applied to the full BCU sample. Among 1420 BCUs, 825 are classified as BL Lac candidates and 405 as FSRQ candidates, while 190 sources remain without a firm label. As a result, the BCU fraction in the catalog is reduced from 39.9% to about 5%, making the resulting catalog more suitable for statistical population studies, spectroscopic follow-up planning, and multiwavelength source selection.

Chapter 3

In the third section a machine learning framework for one-zone SSC modeling of blazar SEDs is developed. In the one-zone SSC scenario, the same electron population produces the low-energy synchrotron component and the high-energy inverse-Compton component by scattering the synchrotron photons. When this model is used to model the SED, it becomes computationally expensive when particle injection and cooling are included, because the coupled evolution of electrons and photons, together with cooling and pair-production effects, must be solved numerically for each parameter set.

To overcome this difficulty, a CNN is trained on a large library of SSC spectra generated with the *SOPRANO* kinetic code. The training dataset consists of 2×10^5 simulated spectra spanning a broad range of physically relevant SSC parameters, including Doppler factors $3 < \delta < 50$, emission region sizes $10^{15} < R < 10^{18}$, cm, minimum and maximum electron Lorentz

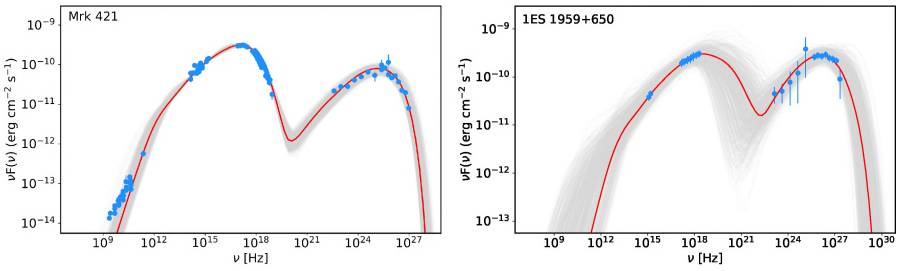

Figure 3: The broadband SEDs of Mrk 421 during the 4.5-month-long multi-wavelength campaign in 2009 (left) and of 1ES 1959+650 on the 14$^{\text{th}}$ of June 2016 (right). The data and its errors are in blue, the red line is the model corresponding to the best parameters, i.e., maximizing the likelihood, and the grey spectra represent one in 10 randomly selected samples from the MCM sampling, representing the model uncertainty. The data are corrected for EBL absorption.

factors $10^{1.5} < \gamma_{\rm min} < 10^5$ and $10^2 < \gamma_{\rm max} < 10^8$, electron injection indices $1.8 < p < 5$, electron luminosities $10^{42} < L_{\rm e} < 10^{48}, {\rm erg, s^{-1}}$, and magnetic field strengths $10^{-3} < B < 10^2, {\rm G}$. The network learns the relation between these seven physical model parameters and the emitted broadband spectrum sampled in 150 energy bins. After training, the surrogate reproduces the numerical spectra with high accuracy while reducing the evaluation time from about 10–100 seconds to about 10^{-2}–10^{-3} seconds. This speedup makes it practical to use the SSC model within Bayesian inference when fitting observational data.

The performance of the method is demonstrated by connecting the CNN with MultiNest and modeling the broadband SEDs of Mrk 421 and 1ES 1959+650. Figure 3 shows the observed data together with the best-fit SSC spectra. In both cases the CNN reproduces the broadband shape well and makes it possible to explore the posterior distribution efficiently. For Mrk 421, the fit gives $p = 2.16 \pm 0.04$, $\log_{10}(\gamma_{\rm max}) = 5.40 \pm 0.17$, $\delta = 23.88 \pm 6.54$, $\log_{10}(B/[{\rm G}]) = -1.06 \pm 0.22$, and $\log_{10}(R/[{\rm cm}]) = 15.72 \pm 0.37$. The inferred electron and magnetic luminosities, $\log_{10}(L_{\rm e}/[{\rm erg\,s^{-1}}]) = 42.88 \pm 0.12$ and $\log_{10}(L_{\rm B}/[{\rm erg s^{-1}}]) = 41.66$, indicate a system relatively close to equipartition. For 1ES 1959+650, the all-free fit gives a lower magnetic field, $\log_{10}(B/[{\rm G}]) = -2.16 \pm 0.49$, a larger emitting region, $\log_{10}(R/[{\rm cm}]) = 16.89 \pm 0.52$, and $\delta = 14.13 \pm 10.22$. The fitted parameters are summarized together with the Mrk 421 results in Table 2.

These results demonstrate that the CNN surrogate can reproduce the

Table 2: Parameters describing the SEDs in Figure 3.

Parameters	Mrk 421	1ES 1959+650
p	2.16 ± 0.04	2.12 ± 0.16
$\log_{10}(\gamma_{\rm max})$	5.40 ± 0.17	6.87 ± 0.33
$\log_{10}(\gamma_{\rm min})$	2.57 ± 0.17	2.56 ± 0.62
δ	23.88 ± 6.54	14.13 ± 10.22
$\log_{10}(B/[\rm G])$	-1.06 ± 0.22	-2.16 ± 0.49
$\log_{10}(R/[\rm cm])$	15.72 ± 0.37	16.89 ± 0.52
$\log_{10}(L_{\rm e}/[\rm erg\ s^{-1}])$	42.88 ± 0.12	43.98 ± 0.40
$\log_{10}(L_{\rm B}/[\rm erg\ s^{-1}])$	41.66	41.34

observed broadband SEDs and recover physically meaningful regions of the model parameter space. They also show that the method can be combined with Bayesian inference to constrain SSC model parameters efficiently.

Chapter 4

In the fourth chapter the SSC modeling framework is applied to model the SEDs of PKS 2155-304, a high-synchrotron-peaked BL Lac at redshift $z = 0.117$. The source is highly variable from optical/UV to X-ray and γ-ray energies, and its long observational history makes it suitable for systematic time-resolved modeling. The time-resolved SEDs are constructed using the Bayesian-block segmentation of the *Fermi*-LAT light curve, with data from other wavebands grouped to maximize quasi-simultaneity. This approach is important because blazar emission vary rapidly, and SEDs built from non-simultaneous data can mix physically different states. The resulting SED sequence shows that the synchrotron peak of PKS 2155-304 remains around $\nu_{\rm s} \simeq (1\text{–}5) \times 10^{16}$ Hz, while the flux level and spectral curvature change substantially across the different activity states.

The segmentation results in the construction of 253 quasi-simultaneous SEDs for different emission periods of PKS 2155-304. Based on their multiwavelength characteristics, these SEDs are grouped into quiescent (QS), multiwavelength-flaring (MWF), γ-ray-flaring (γF), X-ray-flaring (XF), and optical/UV-flaring (OUF) states. Then each SED is modeled with the same one-zone SSC framework described in the Chapter 3, allowing a homogeneous comparison of the inferred physical parameters. The inferred

Table 3: Results of the KS test, indicating if the parameter variation between any state and the QS are significant. The parameters are in this order: magnetic field (B), electron luminosity (L_e), maximum energy ($\gamma_{\rm max}$), emission region size (R), Doppler factor (δ), spectral index (p).

State	B		L_e		$\gamma_{\rm max}$		R		δ		p	
	KS	p	KS	p	KS	p	KS	p	KS	p	KS	p
MWF	0.338	0.045	0.359	0.027	0.474	1.0×10^{-3}	0.252	0.236	0.410	0.007	0.137	0.899
γF	0.267	0.354	0.293	0.254	0.327	0.155	0.265	0.364	0.239	0.489	0.506	0.004
XF	0.545	3.0×10^{-5}	0.301	0.072	0.338	0.030	0.519	8.8×10^{-5}	0.390	0.008	0.405	0.005
OUF	0.316	0.007	0.381	4.8×10^{-4}	0.418	8.9×10^{-5}	0.143	0.581	0.290	0.016	0.283	0.021

parameters show how changes in the jet conditions are connected to the different multiwavelength activity states.

The Kolmogorov–Smirnov (KS) test is performed to compare the inferred SSC parameter distributions of each active state with the QS distribution, and the statistical comparison is summarized in Table 3. The MWF state differs significantly from QS in magnetic field, electron luminosity, maximum electron energy, and Doppler factor, but not in emitting-region size or electron index. The γF state shows the weakest overall difference from QS, with the only clear difference appearing in the spectral index p, which becomes harder during γ-ray flares. In contrast, the XF state shows the strongest changes, with significant differences in B, $\gamma_{\rm max}$, R, δ, and p, indicating that X-ray flares involve simultaneous changes in magnetization, particle acceleration, and emission geometry. The OUF state also differs from QS in all parameters except R, showing that optical/UV flares are associated with changes in magnetic field, electron properties, and relativistic boosting.

Figure 4 shows a visual summary of these trends through box plots of the parameter distributions. The XF state tends to have larger magnetic fields and broader changes in the emitting-region properties, while γF states favor slightly harder electron spectra together with lower δ and $\gamma_{\rm max}$ than most other states. MWF episodes are characterized by relatively high $\gamma_{\rm max}$ and enhanced L_e, whereas OUF episodes show strong deviations in several parameters but not in the size of the emitting region. This qualitative picture is consistent with the KS-test results and shows that different flare classes are driven by different combinations of physical parameter changes.

Such a change in the parameters, shows that the variability of PKS 2155-304 is not controlled by a single parameter. X-ray flares are most naturally associated with stronger magnetic fields, higher maximum electron energies, and changes in source size and boosting, while γ-ray flares are more closely connected with hardening of the electron distribution. In all

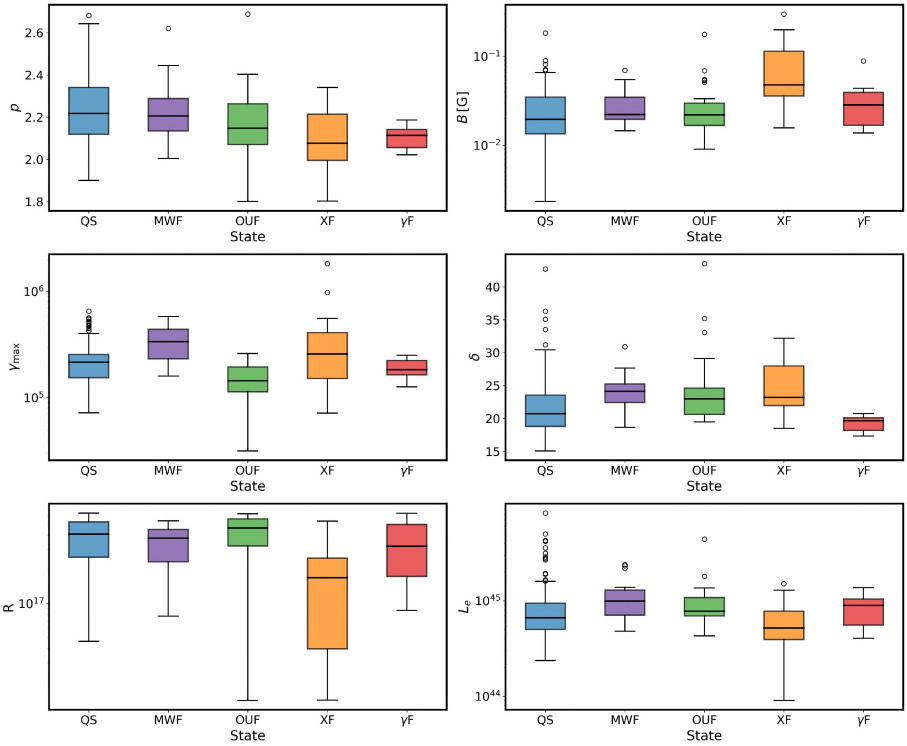

Figure 4: The distributions of all model parameters p, B [G], $\gamma_{\max}$, δ, R [cm] and L_e [erg.s^{-1}] for different states represented as box plots — QS (blue), MWF (violet), OUF (green), XF (orange) and γF (red). The central line marks the median, box edges correspond to the 25th and 75th percentiles, whiskers extend to $1.5\times$ the interquartile range , and outliers are plotted as circles. Qualitatively, the X-ray–flaring state tends to show larger B, while γ-ray-flaring states favor slightly harder p and lower δ and $\gamma_{\max}$ relative to other states.

states, however, the emitting region remains particle dominated, with $\eta_B \simeq 0.09$–0.17. This favors a low-magnetization flow in which shocks or turbulence can accelerate electrons efficiently without requiring a strongly magnetized reconnection-dominated regime.

Chapter 5

In this section, the multiwavelength emission from the FSRQ PKS 1441+25 is investigated during its VHE γ-ray emitting state. Such detections are rare in FSRQs because their accretion disks and broad-line regions (BLRs) produce dense photon fields. If the γ-ray emitting region is located inside or close to the BLR, VHE photons can interact with these low-energy photons through $\gamma\gamma$ pair production, creating electron–positron pairs and preventing the VHE emission from escaping.

For this reason, the detection of VHE γ-rays from PKS 1441+25 is especially important. This source, located at redshift $z = 0.939$, was detected in the VHE band by MAGIC and VERITAS during its 2015 activity, making it a useful case for constraining the location of HE emission along the jet.

The origin of the emission from PKS 1441+25 is investigated using a multiwavelength dataset that includes *Fermi*-LAT γ-ray data, *Swift*-XRT/*Swift*-UVOTand *NuSTAR* observations, optical data, and infrared photometry. An adaptive-binning analysis of the *Fermi*-LAT light curve reveals a prolonged high state beginning around MJD 57000, including a strong HE flare in late January and a harder γ-ray spectrum in April, when VHE emission was detected. To study the emission during this activity, four representative SED intervals are selected: 29–30 January 2015, 24–28 April 2015, 01–15 May 2015, and 01–04 June 2015. These SEDs are fitted with a one-zone external inverse-Compton model evaluated with the CNN surrogate. The resulting SEDs are shown in Figure 5, and the best-fit physical parameters are summarized in Table 4.

The inferred parameters show a clear separation between the January flare and the April–June activity. The January state requires a compact emission region with $\log R = 15.03 \pm 0.91$ and a much stronger magnetic field, $\log B = 0.77 \pm 0.26$, while the three later states all favor large regions with $\log R \simeq 17.1$ and weak magnetic fields with $\log B \simeq -1.7$. The January SED is therefore consistent with a dissipation site inside or near the BLR, where direct disk and BLR photons can affect the VHE component and where

Table 4: Best-fit physical parameters obtained from modeling the SEDs of PKS 1441+25 during the four different periods. For each interval, the table lists the electron injection index p, the cutoff Lorentz factor $\gamma_{\rm cut}$, the Doppler factor δ, the magnetic-field strength B, the radius of the emitting region R, and the electron kinetic luminosity $L_{\rm e}$. The magnetic luminosity $L_{\rm B}$ is computed from the fitted B, R, and δ.

Parameter	29–30 Jan 2015	24–28 Apr 2015	01–15 May 2015	01–04 Jun 2015
p	2.40 ± 0.52	2.41 ± 0.20	2.33 ± 0.29	2.38 ± 0.35
$\log \gamma_{\rm cut}$	3.71 ± 1.21	4.94 ± 0.19	5.04 ± 0.42	4.41 ± 0.96
δ	42.62 ± 8.04	45.36 ± 7.46	32.47 ± 7.85	39.53 ± 6.97
$\log B$	0.77 ± 0.26	-1.66 ± 0.36	-1.74 ± 0.50	-1.79 ± 0.80
$\log R$	15.03 ± 0.91	17.10 ± 0.44	17.17 ± 0.44	17.13 ± 0.52
$\log L_{\rm e}$	44.98 ± 0.83	45.99 ± 0.24	45.92 ± 0.56	46.08 ± 0.58
$\log L_{\rm B}$	44.43	43.77	43.46	43.44

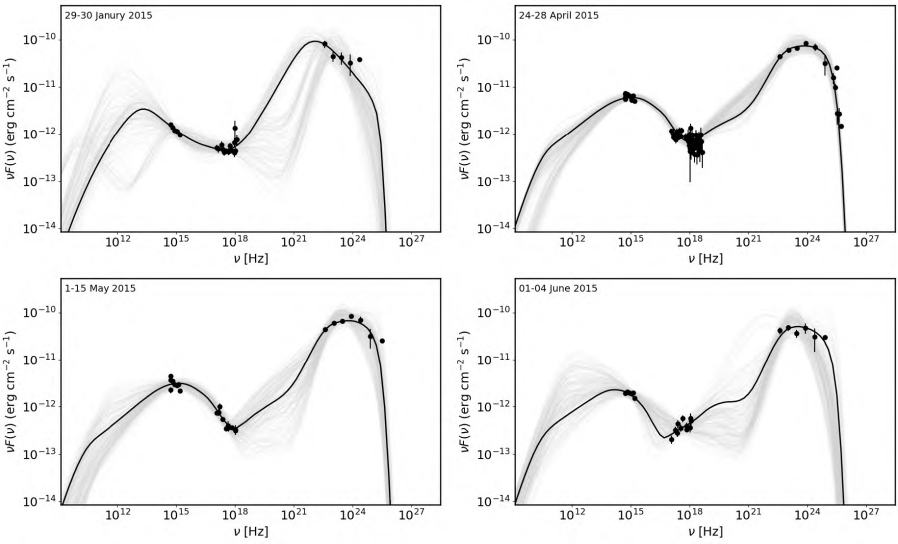

Figure 5: SED of PKS 1441+25 for the four different intervals selected from the multiwavelength light curve: 29-30 January 2015, 24-28 April 2015, 01-15 May 2015, and 01-04 June 2015. Black points show the contemporaneous multiwavelength data used in each fit. The solid black curve in each panel represents the best-fit one-zone EIC model obtained with the CNN-accelerated inference framework, while the grey curves correspond to random posterior realizations from the MultiNest sampling.

internal $\gamma\gamma$ absorption naturally suppresses VHE emission.

By contrast, the April, May, and June SEDs are all reproduced with large emitting regions, weak magnetic fields, and electron kinetic luminosities around $\log L_{\rm e} \simeq 46$. These conditions place the emission region beyond the BLR, where the dusty torus becomes the dominant external photon field and VHE photons can escape. The April interval, which corresponds to the VHE-detection period, combines a large region with $\log R = 17.10 \pm 0.44$, a Doppler factor of 45.36 ± 7.46, and a high cutoff energy $\log \gamma_{\rm cut} = 4.94 \pm 0.19$, allowing the inverse-Compton component to extend to VHE energies.

The May and June states remain broadly similar to April, confirming that the source stays in a particle-dominated, Compton-dominated regime after the emission region has moved downstream. In May, the fitted cutoff energy reaches $\log \gamma_{\rm cut} = 5.04 \pm 0.42$, while in June the electron kinetic luminosity rises to $\log L_{\rm e} = 46.08 \pm 0.58$ and the Doppler factor remains high at 39.53 ± 6.97. In all three later epochs, the magnetic luminosity stays almost an order of magnitude below the electron luminosity, whereas in January the stronger magnetic field makes the source much closer to equipartition.

These results suggest an evolutionary scenario. The January activity corresponds to an upstream dissipation episode, where disk and BLR photons dominate the external radiation field. By contrast, the April–June activity corresponds to a later downstream phase, in which the emission region has moved beyond the BLR and interacts mainly with photons from the dusty torus. This evolution naturally explains the observed differences in Compton dominance, spectral hardness, and VHE transparency without requiring a change in the basic radiation mechanism.

Publications in the topic of the thesis

The thesis is connected with peer-reviewed publications and related works including:

1. N. Sahakyan, V. Vardanyan, and **M. Khachatryan**, "Gradient boosting decision trees classification of blazars of uncertain type in the fourth Fermi-LAT catalogue", Monthly Notices of the Royal Astronomical Society, 519(2), 3000–3010 (2023), https://doi.org/10.1093/mnras/stac3701.

2. D. Bégué, N. Sahakyan, H. Dereli-Bégué, P. Giommi, S. Gasparyan, **M.**

Khachatryan, A. Casotto, and A. Pe'er, "Modeling Blazar Broadband Emission with a Convolutional Neural Network. I. Synchrotron Self-Compton Model", The Astrophysical Journal, 963(1), 71 (2024), https://doi.org/10.3847/1538-4357/ad19cf.

3. G. Harutyunyan, N. Sahakyan, D. Bégué, and **M. Khachatryan**, "A comprehensive view of PKS 2155-304 from 2008 to 2023 through a multi-epoch modeling of its spectral energy distributions", Monthly Notices of the Royal Astronomical Society, 546(1) (2026), https://doi.org/10.1093/mnras/staf2282.

4. **M. Khachatryan**, "The origin of multiwavelength emission from PKS 1441+25", Astrophysics, 69(1) (2026), https://doi.org/10.1007/s10511-026-09892-7.

Ամփոփագիր

Բլազարները ակտիվ գալակտիկական միջուկների ամենահզոր և առավել փոփոխական դասերից են, որոնց ռելյատիվիստական շիթերն ուղղված են դեպի դիտողը: Դոպլերյան ուժեղացման հետևանքով դրանց ոչ ջերմային ճառագայթումը դիտվում է էլեկտրամագնիսական սպեկտրի լայն տիրույթում՝ ռադիոալիքներից մինչև բարձր և գերբարձր էներգիաների գամմա տիրույթը: Բլազարների արագ փոփոխականությունը, ճառագայթումը լայն տիրույթում, բևեռացված ճառագայթումը և հնարավոր կապը բարձր էներգիայի նեյտրինոների հետ դրանք դարձնում են կարևոր աստղաֆիզիկական աղբյուրներ՝ ռելյատիվիստական շիթերում մասնիկների արագացման, մագնիսական դաշտերի, ճառագայթման մեխանիզմների, ինչպես նաև շիթ ակրեցիոն սկավառակ փոխազդեցության ուսումնասիրության համար:

Ատենախոսությունը կազմված է ներածությունից, հինգ գլուխներից, եզրակացություններից և օգտագործված գրականության ցանկից:

Ներածությունում ներկայացված են ակտիվ գալակտիկական միջուկների, մասնավորապես՝ բլազարների ուսումնասիրման արդիական խնդիրները, բազմաալիքային և բազմասուրհանդակային աստղաֆիզիկայի նշանակությունը, ինչպես նաև մեքենայական ուսուցման մեթոդների կիրառման հնարավորությունները բլազարների դասակարգման և ճառագայթման մոդելավորման խնդիրներում:

Առաջին գլխում ներկայացված են բլազարների հիմնական դիտողական հատկությունները, ճառագայթման մեխանիզմները և ռելյատիվիստական շիթերում մասնիկների ճառագայթման ֆիզիկական պրոցեսները: Քննարկվել են սինքրոտրոնային, սինքրոտրոնային և արտաքին ֆոտոնային դաշտերի վրա հակադարձ կոմպտոնյան ցրման մոդելները, ինչպես նաև հադրոնային սցենարները: Ներկայացվել են աշխատանքում օգտագործված բազմահաճախային տվյալների հիմնական աղբյուրներն ու մեքենայական ուսուցման մեթոդները:

Երկրորդ գլխում իրականացվել է չդասակարգված բլազարների դասակարգում՝ օգտագործելով Fermi-LAT չորրորդ կատալոգի գամմա-ճառագայթային տիրույթի տվյալները: Բլազարների սպեկտրալ և ժամանակային հատկությունների հիման վրա ուսուցանվել են արհեստական նեյրոնային ցանցեր, ինչպես նաև gradient boosting decision tree տիպի ալգորիթմներ՝ XGBoost և LightGBM: Ստացված արդյունքների հիման վրա իրականացվել է չդասակարգված բլազարների բաժանումը BL Lac և FSRQ

ենթադասերի:

Երրորդ գլխում ներկայացված է convolutional neural network (CNN)-ի վրա հիմնված նոր մեթոդ՝ բլազարների ճառագայթման սպեկտրների արագ մոդելավորման համար: Սինքրոտրոնային ֆոտոնների հակադարձ կոմպտոնյան ցրման մոդելի շրջանակում CNN-ը ուսուցանվել է սինթետիկ տվյալների վրա՝ սովորելով ճառագայթման թվային մոդելի և ֆիզիկական պարամետրերի միջև կապը: Ցույց է տրվել, որ նեյրոնային ցանցը բարձր ճշտությամբ վերարտադրում է թվային հաշվարկներով ստացված սպեկտրները՝ զգալիորեն արագացնելով մոդելավորման գործընթացը: Մոդելը կիրառվել է Mrk 421 և 1ES 1959+650 բլազարների լայնաշերտ սպեկտրների մոդելավորման համար:

Չորրորդ գլխում իրականացվել է PKS 2155-304 բլազարի բազմահաճախային տվյալների ուսումնասիրություն՝ 2008–2023 թվականների ընթացքում: Վերլուծվել են Fermi-LAT, Swift-XRT/UVOT և այլ արխիվային տվյալներ, կառուցվել են տարբեր ակտիվության վիճակներին համապատասխան սպեկտրալ էներգիական բաշխվածություններ: Աղբյուրի ճառագայթումը մոդելավորվել է սինքրոտրոնային ֆոտոնների հակադարձ կոմպտոնյան ցրման մոդելի շրջանակում, գնահատվել են ճառագայթող մասնիկների և շիթը բնութագրող հիմնական պարամետրերի փոփոխությունները տարբեր վիճակներում:

Հինգերորդ գլխում ուսումնասիրվել են PKS 1441+25 բլազարի բազմահաճախային տիրույթում ճառագայթման մեխանիզմները: Օգտագործելով Fermi-LAT, Swift-XRT/UVOT և այլ դիտակներով գրանցված տվյալները՝ կառուցվել են աղբյուրի տարբեր ակտիվության վիճակներին համապատասխան ճառագայթման սպեկտրներ, որոնք մոդելավորվել են լեպտոնային մոդելի շրջանակում՝ հաշվի առնելով սինքրոտրոնային, սինքրոտրոնային ֆոտոնների և արտաքին ֆոտոնային դաշտերի վրա հակադարձ կոմպտոնյան ցրման մեխանիզմները: Գնահատվել են ճառագայթման տիրույթի ֆիզիկական պարամետրերը և քննարկվել դրանց փոփոխությունները բռնկման տարբեր փուլերում:

Резюме

Блазары один из самых мощных и наиболее переменных классов активных ядер галактик, чьи релятивистские джеты направлены в сторону наблюдателя. Из-за эффекта Доплеровского усиления их нетепловое излучение наблюдается в широком диапазоне электромагнитного спектра: от радиоволн до гамма-излучения высоких и сверхвысоких энергий. Быстрая переменность блазаров, широкополосное излучение, поляризация и возможная связь с нейтрино высоких энергий делают их важнейшими астрофизическими объектами для изучения ускорения частиц в релятивистских джетах, магнитных полей, механизмов излучения, а также взаимодействия джета с аккреционным диском.

Диссертация состоит из введения, пяти глав, заключения и списка использованной литературы.

Во введении представлены актуальные проблемы изучения активных ядер галактик, в частности блазаров, значение многоволновой и многоканальной астрофизики, а также возможности применения методов машинного обучения в задачах классификации блазаров и моделирования их излучения.

В первой главе представлены основные наблюдательные свойства блазаров, механизмы излучения и физические процессы излучения частиц в релятивистских джетах. Обсуждаются модели синхротронного излучения, обратного комптоновского рассеяния на синхротронных и внешних фотонных полях, а также адронные сценарии. Представлены основные источники многоволновых данных и методы машинного обучения, использованные в работе.

Во второй главе проведена классификация неклассифицированных блазаров с использованием данных гамма-диапазона из четвертого каталога Fermi-LAT. На основе спектральных и временных характеристик блазаров были обучены искусственные нейронные сети, а также алгоритмы типа градиентного бустинга над деревьями решений: XGBoost и LightGBM. На основе полученных результатов проведено разделение неклассифицированных блазаров на подклассы BL Lac и FSRQ.

В третьей главе представлен новый метод на основе сверточных нейронных сетей (CNN) для быстрого моделирования спектров излучения блазаров. В рамках модели обратного комптоновского рассеяния синхротронных фотонов CNN

была обучена на синтетических данных, изучая связь между численной моделью излучения и физическими параметрами. Показано, что нейронная сеть с высокой точностью воспроизводит спектры, полученные численными расчетами, значительно ускоряя процесс моделирования. Модель была применена для моделирования широкополосных спектров блазаров Mrk 421 и 1ES 1959+650.

В четвертой главе проведено исследование многоволновых данных блазара PKS 2155-304 за период 2008–2023 гг. Проанализированы архивные данные Fermi-LAT, Swift-XRT/UVOT и других инструментов, построены спектральные распределения энергии, соответствующие различным состояниям активности. Излучение источника смоделировано в рамках модели обратного комптоновского рассеяния синхротронных фотонов, оценены изменения основных параметров излучающих частиц и джета в различных состояниях.

В пятой главе изучены механизмы многоволнового излучения блазара PKS 1441+25. С использованием данных, зарегистрированных телескопами Fermi-LAT, Swift-XRT/UVOT и другими инструментами, построены спектры излучения для различных состояний активности источника. Спектры смоделированы в рамках лептонной модели с учетом механизмов синхротронного излучения, а также обратного комптоновского рассеяния на синхротронных фотонах и внешних фотонных полях. Оценены физические параметры области излучения и обсуждены их изменения на различных стадиях вспышек.

Մհեր Խաչատրյան / **Mher Khachatryan** / Мгер Хачатрян